Eur. Phys. J. E (2014) **37**: 107
DOI 10.1140/epje/i2014-14107-1

THE EUROPEAN PHYSICAL JOURNAL E

Regular Article

High-pressure mass transport properties measured by dynamic near-field scattering of non-equilibrium fluctuations*

C. Giraudet, H. Bataller[a], and F. Croccolo

Laboratoire des Fluides Complexes et leurs Réservoirs, UMR 5150, Université de Pau et des Pays de l'Adour, 64600 Anglet, France

Received 19 September 2014 and Received in final form 21 October 2014
Published online: 19 November 2014 –

Abstract. High-pressure mass diffusion and Soret coefficients of the equimassic 1,2,3,4-tetrahydronaphthalene and *n*-dodecane binary mixture are obtained from dynamic light scattering analysis of concentration non-equilibrium fluctuations at the steady state of Soret-driven separation. A high-pressure shadowgraph set-up has been developed to investigate thermodiffusion in free medium from atmospheric pressure up to 20 MPa. Results at atmospheric pressure show excellent agreement with benchmark values. High-pressure results for the mass diffusion coefficient confirm theoretical predictions by Leffler-Cullinan relation. Further calculation of the thermodiffusion coefficient allows also comparison with previous experimental results with, again, very good agreement.

1 Introduction

A macroscopic gradient of the concentration in a binary fluid mixture induces mass diffusion and a temperature gradient by means of the Dufour effect, whereas a temperature gradient induces thermal diffusion and a concentration gradient by means of the Soret effect [1]. A thermodiffusive experiment is typically performed by applying a stabilizing thermal gradient to a multi-component fluid mixture thus obtaining a superposition of the mentioned *phenomena*. Restricting our interest to the mass flux, we can note that the Fick diffusion and the Soret separation act in opposite directions so that for a binary mixture one can write the total flux of the denser component $\vec{J}$ as $\vec{J} = -\rho D[\vec{\nabla}c + S_T c_0(1-c_0)\vec{\nabla}T]$, where ρ is the fluid density, D the mass diffusion coefficient, $\vec{\nabla}c$ the concentration gradient (of the denser component), S_T the Soret coefficient, c_0 the equilibrium concentration of the mixture and $\vec{\nabla}T$ the temperature gradient. After the application of the thermal gradient a transient state characterised by an increasing concentration gradient leads the system towards a stationary state where the flux vanishes and $\vec{\nabla}c = -S_T c_0(1-c_0)\vec{\nabla}T$.

Characterising the mass transport properties of fluid mixtures like D and S_T still represents a real challenge for scientists either form the theoretical, simulation or experimental point of view [2]. From the theoretical point of view the most challenging issue is the lack of a general theory describing the Soret effect. From the experimental side, many techniques are now available [3] and most of them are of optical nature. Recently great effort has been dedicated to understand and obtain measurements on transport properties of mixtures containing three or more components as it is currently done within the international space project DCMIX [4].

Among the available optical techniques, we recently introduced the use of dynamic Near-Field Scattering to investigate the properties of concentration non-equilibrium fluctuations (c-NEFs) to study the transport properties of the mixture [5,6].

A further ingredient is the fact that oil industry is very much interested in getting a better understanding of transport properties of multi-component fluid mixtures in conditions typical of production fields; *i.e.* high pressure (HP) and porous media [7]. Their interest is obviously aimed at increasing the capacity of accurately predicting the distribution of different species in an oil field during its study campaign. One of the obstacles to reach this task is the lack of understanding and/or availability of experimental data for the influence of HP or porous media on transport properties. Our research project thus aims at providing reference experimental data for transport properties of standard fluid mixtures in such conditions [8,9]; *i.e.* performing high-pressure measurements on binary mixtures stressed by a temperature gradient and going through mass diffusion and Soret separation across a porous medium.

In this paper we report our measurements of the mass diffusion and Soret coefficients of a binary mixture in free medium and in a wide pressure range. The liquid

* Contribution to the Topical Issue "Thermal non-equilibrium phenomena in multi-component fluids" edited by Fabrizio Croccolo and Henri Bataller.

[a] e-mail: henri.bataller@univ-pau.fr

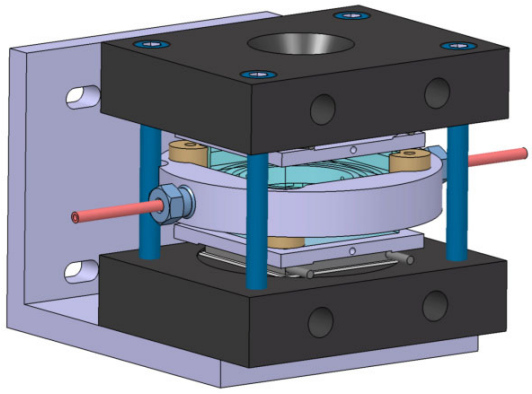

Fig. 1. 3D drawing of the high-pressure cell.

mixture belongs to the well-characterised Fontainebleau benchmark [10] and is an equimassic 1,2,3,4-tetrahydronaphtalene (THN) and n-dodecane (n-C_{12}) at constant temperature $T_{\mathrm{mean}} = 298.15\,\mathrm{K}$.

The remainder of this paper is organized as follow: in sect. 2 the experimental set-up is briefly described, in sect. 3 the theory of non-equilibrium fluctuations is summarized to provide the working equations used in the following, in sect. 4 experimental results are presented and compared with literature data and theoretical models, and finally conclusions are provided in sect. 5.

2 Experimental set-up and procedure

2.1 Experimental set-up

The experimental set-up is quite similar to the one used in previous experiments, so that the reader is addressed to older papers for more details [5,6]. Only the thermodiffusion cell has been significantly modified to allow HP measurements. Consequently, also the filling procedure is changed. In fig. 1 we report a sketch of the high-pressure thermodiffusion cell, specifically designed for applying a vertical temperature gradient with excellent thermal homogeneity and stability to a horizontal thin slab of a multi-component fluid under high pressure while providing vertical optical access to a central area of the cell. The cell core consists of a stainless steel annulus of internal/external diameter 30/75 mm with high-pressure inlet and outlet at its opposite sides. This part accommodates Viton O-rings for sealing and square sapphire plates kept at a distance $L = 5\,\mathrm{mm}$ by the annulus itself, thus defining the sample thickness. In order to minimize the contact between the liquid sample and the conductive metal a Teflon annulus (internal/external diameter 19.8/30 mm) with two thin holes for inlet/outlet of the fluid has been inserted in the inner part of the stainless annulus zone.

Similarly to the ambient-pressure version of the cell, the external sides of the sapphire windows are in thermal contact with two aluminium plates with a central circular aperture ($d = 13\,\mathrm{mm}$), where two thermistors (Wavelenght Electronics, TCS651) are installed to monitor the sapphire temperature. External to the aluminium plates, two Peltier elements (Kryotherm, TB-109-1.4-1.5 CH) with central circular aperture ($d = 13\,\mathrm{mm}$) provide/remove the heat necessary to maintain the set-point temperature as driven by two temperature controllers (Wavelenght Electronics, LFI-3751). Finally, external to the Peltier elements, two aluminium plates are flown with water coming from a thermostatic bath (Huber, ministat 125) to remove the excess heat of the Peltiers.

The filling system for HP measurements consists of: a rotary vacuum pump able to evacuate most of the air from the cell before filling operations down to a residual pressure of about 10 Pa; a fluid vessel at atmospheric pressure; a manual volumetric pump and a number of valves to facilitate the procedure. Briefly, after a low vacuum is made inside the cell, the mixture to be studied is transferred to the cell by acting on the volumetric pump. Visual check allows avoiding bubbles during the injection procedure. After that, the cell is abundantly fluxed with the fluid mixture. At the end of the procedure a valve is closed and the volumetric pump is operated to modify the liquid pressure within the cell. A manometer (Keller, PAA-33X, pressure range: 0.1–100 MPa, precision $\pm 0.04\,\mathrm{MPa}$) is connected between the volumetric pump and the cell to measure the pressure of the fluid mixture. A second identical manometer is connected to the outlet of the cell. The manometer signals are transferred using an acquisition card (National Instruments, NI 9215) interfaced to a computer.

The optical technique of choice is Near-Field Scattering [11–13] by means of a shadowgraph set-up [14,15]. The shadowgraph optical set-up has been slightly modified also and presently involves a low coherence light source (Super Lumen, SLD-MS-261-MP2-SM) connected to a single-mode fibre whose output is collimated by an achromatic doublet lens ($f = 15\,\mathrm{cm}$, $\varphi = 5\,\mathrm{cm}$). The light polarization is set by a fixed linear polarizer just after the collimating lens. A second polarizer after the sample allows setting the beam intensity. A charged coupled device (CCD) camera (IDS, UI-6280SE-M-GL) positioned at a distance $z = (10.0 \pm 0.5)\,\mathrm{cm}$ from the sample plane collects the light. The camera sensor consists of 2448×2048 square pixels with a side of $3.45\,\mu\mathrm{m}$. No further lens is installed between the sample cell and the CCD sensor so that the image plane is at the detector plane itself and the sample is out of focus by a distance z. The camera is able to transfer about 8.2 images per second to the PC connected via a GigE connection. In order to save the images as quickly as possible, storage is made on a solid state disk (SSD).

2.2 Dynamic near-field imaging

Near-field imaging is a family of optical techniques [16–19] based on a similar physical principle. The common idea is that the light scattered by refractive index inhomogeneities within the sample is collected by a pixelated detector together with the (much more intense) transmitted beam in the near field, *i.e.* sufficiently close to overlap on the detector providing interference. In this way the invisible refractive index fluctuations are transformed into

detectable intensity fluctuations and recorded in the form of images. This family includes different techniques like near-field scattering [11,16,18,19], shadowgraph [5,6,14, 15,20–22], Schlieren [15,23,24] where the main difference is the wave vector range they are able to analyse. A series of such images maps both spatial and temporal fluctuations of the refractive index inside the sample which are related to its temperature and concentration fluctuations and can be analysed by means of statistical analysis of the image Fourier transforms. In this case, we apply the Differential Dynamic Algorithm [5,6,13,20,21,23,25, 26] in order to extract the temporal correlation function of c-NEFs. Since this processing requires a heavy computational effort, we make use of custom-made software taking advantage of the parallelization capabilities of a graphic board [27].

Near-field images consist of intensity maps $I(\vec{x},t)$ of the refractive index fluctuations occurring within the sample. Statistical analysis involving bi-dimensional fast Fourier transforms (2D-FFTs) and azimuthal averages provides accurate measurements of the intensity $S(q,t)$ of the light scattered at each wave vector q grabbed by the optical set-up and for all the times t of the acquisition sequence. The dynamic differential algorithm has been demonstrated to provide direct access to the structure function of the sample for all the wave vectors in the optical system by means of a statistical analysis of differences of images. Details of the dynamic analysis can be found elsewhere [5,6,13,20,21,23,25,26]. Here we just recall the working principle and the main equations used to fit experimental data. We define the structure function $C_{\mathrm{NE}}(q,\mathrm{d}t)$ for the given wave vector q and time delay $\mathrm{d}t$:

$$C_{\mathrm{NE}}(q,\mathrm{d}t) = \left\langle \Im \left|\Delta i_m(q,\mathrm{d}t)\right|^2 \right\rangle = 2\left\{S(q)T(q)[1-f(q,\mathrm{d}t)] + B(q)\right\}, \quad (1)$$

where $\Delta i_m(q,\mathrm{d}t)$ is the Fourier transform of the difference of two normalized images temporally separated by a time $\mathrm{d}t$, $S(q)$ the static power spectrum of the sample, $T(q)$ an optical transfer function, $f(q,\mathrm{d}t)$ the intermediate scattering function (ISF) and $B(q)$ a background containing electronic noise but also thermal NEFs, much faster than the acquisition delay time. For many cases of practical interest, the ISF can be safely approximated by a single exponential decay $f(q,\mathrm{d}t) = \exp(-\mathrm{d}t/\tau(q))$ so that eq. (1) takes the form

$$C_{\mathrm{NE}}(q,\mathrm{d}t) = 2\left\{S(q)T(q)[1-\exp(-\mathrm{d}t/\tau(q))] + B(q)\right\}. \quad (2)$$

Fitting the structure function by means of eq. (2) with $S(q)T(q)$, $\tau(q)$ and $B(q)$ as free fitting parameters for each wave vector allows determining the time constants $\tau(q)$. Remarkably, since this analysis takes into account only the temporal evolution of NEFs, this is the only optical technique that does not need knowledge of the so-called optical contrast factors $\partial n/\partial c$ and $\partial n/\partial T$ [28,29] very difficult to obtain in HP conditions.

3 Non-equilibrium fluctuations

NEFs are tiny (in intensity) but giant (in lateral size) fluctuations of the thermodynamic variables that are universally related to the presence of gradients. A description of the theory of NEFs can be found in the nice book by Ortiz de Zárate and Sengers [30]. Here we briefly recall the essential equations that describe the time decay of c-NEFs in the presence of the terrestrial gravitational field and neglecting the action of confinement.

As stated before, the temporal correlation function of c-NEFs is expected to be a single exponential decay for all wave vectors, with time constants $\tau(q)$ varying as a function of q. For wave vectors larger than a characteristic wave vector q_s^*, the decay time is the diffusive one $\tau(q) = 1/(Dq^2)$, while for wave vectors smaller than q_s^*, buoyancy leads to a quadratic dependence of the decay time with respect to the wave vector $\tau(q) = q^2\nu/(\beta g \nabla c)$.

The characteristic wave vector q_s^* is related to fluid parameters and the gravitational field as [31]

$$q_s^* = \left(\frac{\beta_s \vec{g}\cdot\vec{\nabla}c}{\nu D}\right)^{1/4}, \quad (3)$$

where $\beta_s = (1/\rho)(\partial\rho/\partial c)$ is the solutal expansion coefficient, $\vec{g}$ is the gravitational acceleration, and ν is the kinematic viscosity.

Over the entire wave vector range, the decay time is expressed by a characteristic bell-shape curve:

$$\tau(q) = \frac{1}{Dq^2\left[1+(q_s^*/q)^4\right]}. \quad (4)$$

This has been experimentally verified in a number of papers by means of similar approach [5,6,20,21,23]. The combined effect of mass diffusion and gravity (or diffusion only, in space experiments) has been measured also by ultra-low-angle static light scattering machine and shadowgraph [32–35].

Similar reasoning can be applied also to thermal fluctuations, leading to analogous equations. Here, however, we are interested in the analysis of the concentration components, the thermal ones being too fast to be investigated by our optical set-up essentially due to the limited frame rate of the CCD camera. Since the concentration gradient can be written in terms of the temperature gradient and the Soret coefficient, the characteristic wave vector can be written as

$$q_s^* = \sqrt[4]{\frac{\beta g \Delta T S_T c_0(1-c_0)}{L\nu D}}. \quad (5)$$

By inverting eq. (5), one can derive an expression of the Soret coefficient S_T as a function of the (measurable) characteristic wave vector q_s^*, of the mass diffusion coefficient D and of the other (known) fluid properties [5,6]

$$S_T = \frac{{q_s^*}^4 \nu D L}{\beta g \Delta T c_0(1-c_0)}. \quad (6)$$

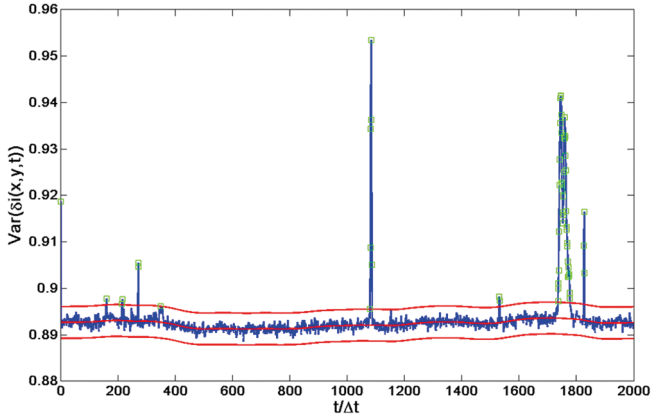

Fig. 2. Variance of the differences of successive images for a typical set (blue line). Undesired peaks can be detected for which the contrast exceed 3 times the variance RMS, thus allowing detection of "problematic" images (green squares).

4 Results and discussion

4.1 Experimental conditions

A series of experimental runs with different pressures have been performed with a binary mixture of 1,2,3,4-tetrahydronaphthalene and *n*-dodecane (THN/*n*-C12) at equimassic concentration. The mean temperature is 298.15 K and the applied temperature difference ΔT = 20 K for all the runs. The sample consists of a layer of L = 5 mm and a lateral size given by the containing Teflon annulus which internal diameter is about $\varphi = 19.8$ mm. For each pressure value, 5 series of 2000 images each have been acquired with an acquisition time delay $\Delta t = (150 \pm 1)$ ms. Each dataset has then been processed on a dedicated PC with custom-made software in order to perform parallel processing of the images to get the structure functions for all the wave vectors and for all the time delays accessible within the image dataset [27].

With respect to precedent versions of the software we have now implemented a preliminary check of the images performed prior to calculate the image FFTs. The goal of this step of analysis is to automatically detect "problematic" images and to exclude them from the calculations. "Problematic" images are typically generated by a dust particle moving in the beam path of the optical set-up thus generating a moving fringe pattern which has nothing to do with the signal of interest. We therefore calculate the variance of each difference of two successive images $\mathrm{Var}(t) = \mathrm{Var}(\delta i(x,y,t)) = \langle [i(\vec{x},t) - i(\vec{x},t+\Delta t)]^2 \rangle_{\vec{x}}$ and then analyse it as a function of time. A typical plot of $\mathrm{Var}(t)$ is shown in fig. 2 where one can clearly detect the presence of peaks of the contrast. To automatically detect these peaks we calculate the variance root mean square (RMS) and define a "problematic" image as an image whose variance is outside 3 times the RMS and set its weight to zero, whereas for "normal" images it is set to unity.

After filling the cell and increasing the pressure to the desired value, the system is let stabilize at the average temperature of 298.15 K for about 5 hours before applying the temperature difference of 20 K via the two distinct temperature controllers. A linear temperature gradient sets up in a time of the order of 100 seconds. The image acquisition is then started about 12 hours after the application of the difference of temperature to be sure that the concentration gradient due to the Soret effect is fully developed.

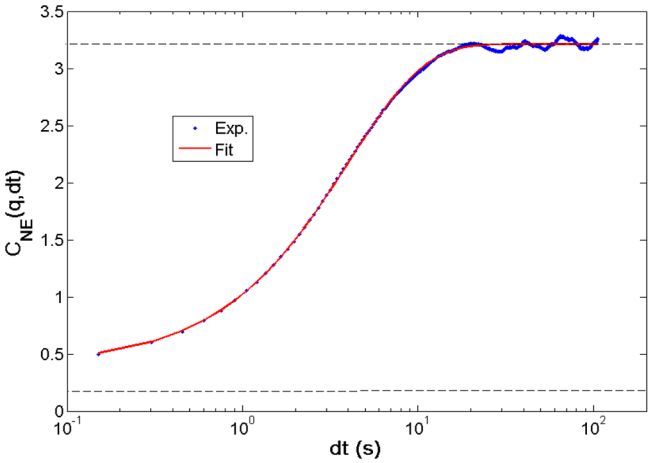

Fig. 3. Structure function $C_{\mathrm{NE}}(q, \mathrm{d}t)$ *vs.* time delay for wave vector $q = 169\,\mathrm{cm}^{-1}$. Continuous red line indicates the fitting function. Data points refer to the following experimental conditions: sample THN/*n*-C12, $c_0 = 50\%$ w/w, $T_{\mathrm{top}} = 308.15$ K, $T_{\mathrm{bottom}} = 288.15$ K, $P = 0.1$ MPa and image delay time $\Delta t = 150$ ms.

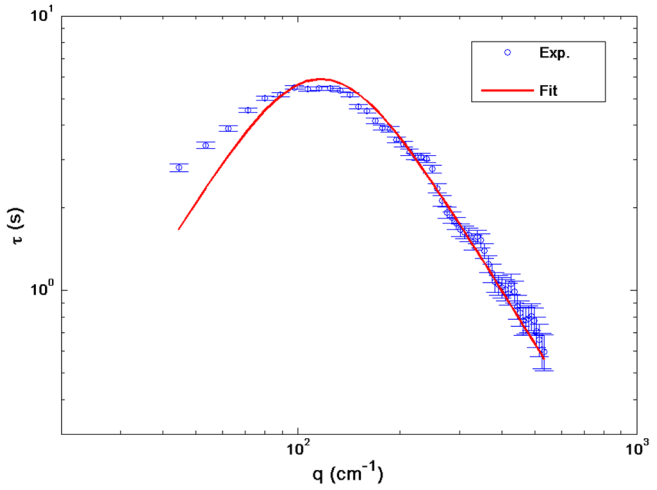

Fig. 4. Time constant $\tau(q)$ *vs.* wave vector q: points are for experimental data, whereas the red continuous line is for the fitting function as per eq. (4). Data points refer to the same experimental conditions as fig. 3.

4.2 Analysis of non-equilibrium fluctuations

In fig. 3 a typical structure function is shown as a function of the time delay between images for one wave vector $q = 169\,\mathrm{cm}^{-1}$ at atmospheric pressure. One can easily detect

Table 1. Experimental values of the diffusion coefficient D, Soret coefficient S_T and thermodiffusion coefficient D_T *vs.* pressure.

P (MPa)	D (10^{-10} m^2/s)	S_T (10^{-3} 1/K)	D_T (10^{-12} m^2/(s K))
0.11	6.25 ± 0.01	9.3 ± 0.5	5.8 ± 0.3
1.06	6.13 ± 0.02	8.5 ± 0.4	5.2 ± 0.3
2.49	6.06 ± 0.01	9.1 ± 0.4	5.5 ± 0.2
3.75	6.01 ± 0.04	9.4 ± 0.5	5.7 ± 0.4
5.07	5.89 ± 0.01	9.0 ± 0.5	5.3 ± 0.3
10.30	5.64 ± 0.04	8.8 ± 0.4	5.0 ± 0.2
20.21	5.05 ± 0.05	8.0 ± 0.7	4.1 ± 0.4

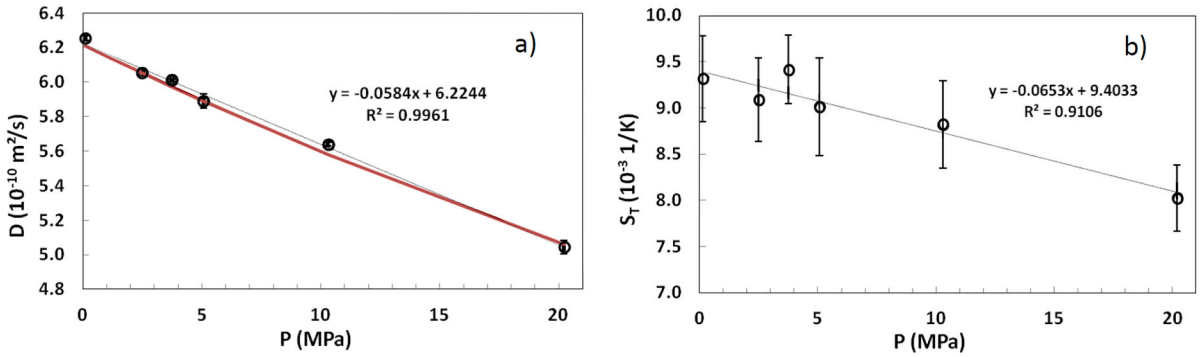

Fig. 5. a) Diffusion coefficient D and b) Soret coefficient S_T *vs.* pressure for the THN/*n*-C12, $c_0 = 50\%$ w/w mixture at 298.15 K: circles are for experimental data, whereas the continuous red line for panel a) stands for estimation by means of eq. (7). In both figures the thin lines show a linear regression of the experimental data.

the amplitude set by the term $S(q)T(q)$ and the starting value given the background $B(q)$ for $\mathrm{d}t \to 0$.

For each set of images structure functions are fitted by means of eq. (2) with $S(q)T(q)$, $\tau(q)$ and $B(q)$ as free fitting parameters for each wave vector. In fig. 4 decay times $\tau(q)$ are shown as a function of the wave vector q for the experiment at atmospheric pressure, together with the result of fitting by eq. (4) (solid line). Values of the diffusion coefficient D and the critical wave vector q_s^* are obtained for each run.

Uncertainties in fig. 4 are the standard deviation from mean value of the time constants calculated from five different experiments per each pressure value.

4.3 Mass diffusion and Soret coefficients

Solutal expansion coefficient and viscosity under high pressure for the THN/*n*-C12 mixture have been measured in previous works [9,36]. From the values of D, q_s^* and known fluid parameters the Soret coefficients can be calculated by means of eq. (6) for each experimental run. The values for each set of measurements at the same pressure are then averaged. In fig. 5 the averaged values of D and S_T as a function of the pressure are shown.

At atmospheric pressure we found values of $D = (6.25 \pm 0.01) \times 10^{-10}$ m^2/s and $S_T = (9.3 \pm 0.5) \times 10^{-3}$ K^{-1} confirming the results obtained in previous measurements with an atmospheric pressure cell [5,6], as well as well-established benchmark values [10].

In fig. 5a also a theoretical prediction by a Leffler-Cullinan relation [37] is plotted. This equation is used to make an evaluation of the molecular diffusion coefficient in free media D as a function of the pressure:

$$D(P) \times \mu(P) \approx \text{constant}, \tag{7}$$

where μ is the dynamic viscosity of the fluid.

At atmospheric pressure and with the literature value for D, we evaluate the constant in eq. (7). The continuous red line in fig. 5a represents then the evaluated values of diffusion coefficient in free media D thanks to the measured values of viscosity [9,36]. The agreement with the presently measured values of D is excellent. A linear regression is shown in the graph as a thin line, along with resulting equation.

The values of the Soret coefficient presented in fig. 5b present a larger error due to the 4th power in eq. (5) and are relatively scattered. However, a decrease of the value of S_T as a function of pressure can be detected. Again, a linear regression is shown as a thin line, together with the resulting equation. Experimental data for S_T and D are reported in table 1.

In fig. 6 we report the values of the thermodiffusion coefficient D_T as evaluated by using

$$D_T = S_T \times D. \tag{8}$$

The red line represents a linear fit of reference D_T values measured with an HP thermogravitational column [38], whereas the thin line is a linear fit of our values of D_T.

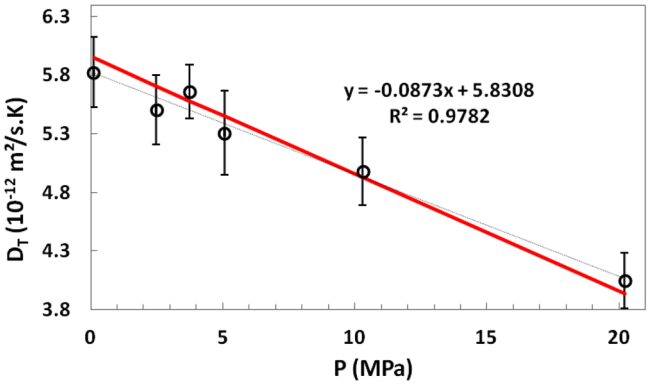

Fig. 6. Thermodiffusion coefficient *vs.* pressure for the THN/*n*-C12, $c_0 = 50\%$ w/w mixture at an average temperature of 298.15 K: circles are for experimental data, whereas the continuous red line stands for references values [38].

The agreement between our data points and the reference data is very good taking into account the experimental errors on D and S_T. We confirm a decrease of the value of the D_T as a function of the pressure. Calculated values of the thermodiffusion coefficient D_T from our experimental data are also reported in table 1.

5 Conclusions

A high-pressure shadowgraph set-up has been developed to measure mass diffusion and Soret coefficients under high pressure. Acquired images are analysed by means of the differential dynamic analysis leading to the retrieval of the time decay for each wave vector and ultimately to the mass diffusion D and Soret S_T coefficients of the analysed binary mixture. Calibration tests of the set-up and procedure have been performed at atmospheric pressure with the THN/*n*-C12 equimassic mixture. High-pressure measurements have been performed up to 20 MPa. The evolution of D as a function of the pressure is in good agreement with the theoretical predictions given by a Leffler-Cullinan relation. A slight decrease of the value of S_T as a function of the pressure is detected.

From the obtained values of D and S_T, the thermodiffusion coefficient D_T can be calculated, too. These values are compared with those obtained by the group of Bou-Ali by means of a high-pressure thermogravitational column, showing very good agreement.

An important point of the measurement technique proposed here is that it is totally non-invasive, whereas the thermogravitational technique requires liquid sampling, which is rather problematic at high pressure. Also, unlike other optical methods, our technique does not need knowledge of optical contrasts factors. Finally, this work confirms that the proposed experimental technique can be considered a sound approach for the study of thermodiffusion process also under high-pressure conditions.

We thank J.M. Ortiz de Zárate from the Universidad Complutense de Madrid for helpful discussions and G. Galliero and G. Pijaudier-Cabot from LFC-R for financial support. We are grateful to L. Marlin, head of the University of Pau workshop, for his help in designing the high-pressure cell.

References

1. S. de Groot, P. Mazur, *Non-Equilibrium Thermodynamics* (Dover, New York, 1984).
2. M.J. Assael, A.R.H. Goodwin, V. Vesovic, W.A. Wakeham, *Experimental Thermodynamics*, Vol. IX, *Advances in Transport Properties of Fluids* (The Royal Society of Chemistry, Cambridge, 2014).
3. J.K. Platten, J. Appl. Mech. **73**, 5 (2006).
4. A. Mialdun, C. Minetti, Y. Gaponenko, V. Shevtsova, F. Dubois, Micrograv. Sci. Technol. **25**, 83 (2013).
5. F. Croccolo, H. Bataller, F. Scheffold, J. Chem. Phys. **137**, 234202 (2012).
6. F. Croccolo, F. Scheffold, H. Bataller, C. R. Méc. **341**, 378 (2013).
7. S. Van Vaerenbergh, A. Shapiro, G. Galliero, F. Montel, J. Legros, J. Caltagirone, J.-L. Daridon, M.Z. Saghir, *Multicomponent Processes in Crudes*, European Space Agency Special Publication 1290 (2005) pp. 202-213.
8. F. Croccolo, H. Bataller, G. Pijaudier-Cabot, AIP Conf. Proc. **1254**, 157 (2010).
9. C. Giraudet, F. Croccolo, G. Galliero, G. Pijaudier-Cabot, S.V. Vaerenbergh, M.Z. Saghir, F. Montel, H. Bataller, C. R. Méc. **341**, 340 (2013).
10. J.K. Platten, M.M. Bou-Ali, P. Costesèque, J.F. Dutrieux, W. Köhler, C. Leppla, S. Wiegand, G. Wittko, Philos. Mag. **83**, 1965 (2003).
11. M. Giglio, M. Carpineti, A. Vailati, Phys. Rev. Lett. **85**, 1416 (2000).
12. R. Cerbino, A. Vailati, Curr. Opin. Colloid Interface Sci. **14**, 416 (2009).
13. F. Giavazzi, R. Cerbino, J. Opt. **16**, 083001 (2014).
14. S.P. Trainoff, D.S. Cannell, Phys. Fluids **14**, 1340 (2002).
15. F. Croccolo, D. Brogioli, Appl. Opt. **50**, 3419 (2011).
16. F. Ferri, D. Magatti, D. Pescini, M.A.C. Potenza, M. Giglio, Phys. Rev. E **70**, 041405 (2004).
17. R. Cerbino, F. Scheffold, Curr. Opin. Colloid Interface Sci. **12**, 50 (2007).
18. D. Brogioli, F. Croccolo, V. Cassina, D. Salerno, F. Mantegazza, Opt. Express **16**, 20272 (2008).
19. D. Brogioli, D. Salerno, V. Cassina, S. Sacanna, A.P. Philipse, F. Croccolo, F. Mantegazza, Opt. Express **17**, 1222 (2009).
20. F. Croccolo, D. Brogioli, A. Vailati, M. Giglio, D.S. Cannell, Ann. N.Y. Acad. Sci. **1077**, 365 (2006).
21. F. Croccolo, D. Brogioli, A. Vailati, M. Giglio, D.S. Cannell, Phys. Rev. E **76**, 41112 (2007).
22. G.S. Settles, *Schlieren and Shadowgraph Techniques: Visualizing Phenomena in Transparent Media* (Springer-Verlag, Berlin, Heidelberg, New York, 2001).
23. F. Croccolo, D. Brogioli, A. Vailati, M. Giglio, D.S. Cannell, Appl. Opt. **45**, 2166 (2006).
24. D. Brogioli, A. Vailati, M. Giglio, Europhys. Lett. **63**, 220 (2003).
25. R. Cerbino, V. Trappe, Phys. Rev. Lett. **100**, 188102 (2008).

26. D. Magatti, M.D. Alaimo, M.A.C. Potenza, F. Ferri, Appl. Phys. Lett. **92**, 241101 (2008).
27. G. Cerchiari, F. Croccolo, F. Cardinaux, F. Scheffold, Rev. Sci. Instrum. **83**, 106101 (2012).
28. F. Croccolo, M.A. Arnaud, D. Bégué, H. Bataller, J. Chem. Phys. **135**, 034901 (2011).
29. F. Croccolo, F. Plantier, G. Galliero, G. Pijaudier-Cabot, M.Z. Saghir, F. Dubois, S. Van Vaerenbergh, F. Montel, H. Bataller, Rev. Sci. Instrum. **82**, 126105 (2011).
30. J.M. Ortiz de Zarate, J.V. Sengers, *Hydrodynamic Fluctuations in Fluids and Fluid Mixtures* (Elsevier Science, New York, 2006).
31. F. Croccolo, H. Bataller, F. Scheffold, Eur. Phys. J. E **37**, 105 (2014).
32. A. Vailati, M. Giglio, Phys. Rev. Lett. **77**, 1484 (1996).
33. A. Vailati, M. Giglio, Nature **390**, 262 (1997).
34. A. Vailati, R. Cerbino, S. Mazzoni, C.J. Takacs, D.S. Cannell, M. Giglio, Nat. Commun. **2**, 290 (2011).
35. C.J. Takacs, A. Vailati, R. Cerbino, S. Mazzoni, M. Giglio, D.S. Cannell, Phys. Rev. Lett. **106**, 244502 (2011).
36. H. Bataller, C. Miqueu, F. Plantier, J.-L. Daridon, T.J. Jaber, A. Abbasi, M.Z. Saghir, M.M. Bou-Ali, J. Chem. Eng. Data **54**, 1710 (2009).
37. J. Leffler, H.T. Cullinan Jr., Ind. Eng. Chem. Fundam. **9**, 84 (1970).
38. P. Urteaga, M.M. Bou-Ali, D. Alonso de Mezquia, J. Santamaría, C. Santamaría, J. Madariaga, H. Bataller, Rev. Sci. Instrum. **83**, 074903 (2012).